SIAM J. SCI. COMPUT.
Vol. 46, No. 6, pp. B806–B829

A SIMULATION METHOD FOR THE WETTING DYNAMICS OF LIQUID DROPLETS ON DEFORMABLE MEMBRANES*

MARCEL MOKBEL†, DOMINIC MOKBEL†, SUSANNE LIESE‡, CHRISTOPH WEBER‡, AND SEBASTIAN ALAND†§

Abstract. Biological cells utilize membranes and liquid-like droplets, known as biomolecular condensates, to structure their interior. The interaction of droplets and membranes, despite being involved in several key biological processes, is so far little understood. Here, we present a first numerical method to simulate the continuum dynamics of droplets interacting with deformable membranes via wetting. The method combines the advantages of the phase-field method for multiphase flow simulation and the arbitrary Lagrangian-Eulerian method for an explicit description of the elastic surface. The model is thermodynamically consistent, coupling bulk hydrodynamics with capillary forces, as well as bending, tension, and stretching of a thin membrane. The method is validated by comparing simulations for single droplets to theoretical results of shape equations, and its capabilities are illustrated in two- and three-dimensional axisymmetric scenarios.

Key words. biomembrane, wetting, two-phase flow, phase field

MSC codes. 35R35, 76M10, 76T30, 74K15

DOI. 10.1137/24M1641142

1. Introduction.

Liquid droplets provide a mechanism for the spatial organization in living cells [68, 9, 11]. These droplets, referred to as biomolecular condensates, arise from condensation of protein-rich material through liquid-liquid phase separation. Examples of such condensates are nucleoli, Cajal bodies, P-bodies, and stress granules [11, 16, 9]. One particularly interesting aspect of biomolecular condensates is their interaction with biological membranes and vesicles via wetting [16, 80]. Recent studies suggest that membrane-droplet interactions are involved in several key biological processes [15, 69, 41, 10, 70, 20]. Understanding the dynamics of wetting of biomolecular condensates on biological membranes requires developing a physical model for the interplay between liquid droplets and deformable surfaces.

When a droplet and a membrane interact, surface tension σ_f causes a reduction in liquid/liquid surface area, which is typically achieved by increasing membrane curvature. This is counteracted by the bending rigidity K_B and the balance of the two determines the elastocapillary length scale $\sqrt{K_B/\sigma_\mathrm{f}}$ of the observed curvature radius [42, 52, 27, 46]. Subsequently, membrane bending results in an apparent contact angle that deviates from droplets wetting a planar surface. Theoretical descriptions of membrane-droplet interactions were studied focusing on equilibrium configurations

*Submitted to the journal's Software, High-Performance Computing, and Computational Science and Engineering section February 22, 2024; accepted for publication (in revised form) July 3, 2024; published electronically November 4, 2024.

https://doi.org/10.1137/24M1641142

Funding: The fifth author received support from the German Research Foundation (grant AL1705/5).

†Faculty of Mathematics and Informatics, TU Freiberg, 09599 Freiberg, Germany (marcel.mokbel@math.tu-freiberg.de, sebastian.aland@math.tu-freiberg.de).

‡Faculty of Mathematics, Natural Sciences, and Materials Engineering, Institute of Physics, University of Augsburg, 86159 Augsburg, Germany (susanne.liese@physik.uni-augsburg.de, christoph.weber@physik.uni-augsburg.de).

§Faculty of Informatics/Mathematics, HTW Dresden, 01069 Dresden, Germany, and Center for Systems Biology Dresden, 01307 Dresden, Germany (sebastian.aland@htw-dresden.de).

and single droplets interacting with one vesicle [42, 43]. A full numerical method to simulate the wetting dynamics on deformable membranes is yet missing.

Even in the absence of wetting, the continuum description of a moving elastic membrane is a highly nonlinear, nonlocal moving boundary problem. Over the past 15 years, various mathematical modeling approaches have been proposed to describe deformable surfaces immersed in a fluid, including immersed boundary methods [35, 67, 56], level-set methods [39, 64], mesh-free methods [61], particle methods [54, 31], and the phase-field method [6]. Nowadays, efficient and unconditionally stable methods exist [13, 76, 29, 77]. In addition, in the last decade numerical methods to simulate wetting on rigid structures have matured, yielding higher order and energy stable schemes to describe complex engineering applications [66, 78, 81, 38, 5]. However, the combination of these two fields, namely the continuum simulation of wetting of deformable membranes, is so far unexplored. Computational methods are currently limited to molecular dynamics simulations which fail to simulate the most relevant time and length scales [44, 26], and a gradient descent minimization of surface energies [65], which fails to produce the correct time evolution or hydrodynamics. To our knowledge, only one preliminary attempt has been made to construct a dynamic simulation method [57]. This approach, based on the lattice Boltzmann method, was however not tailored to fluidic biological membranes, turned out to be relatively unstable and inaccurate, and produced spurious phases and a temporal lag between membrane and fluid movement.

In this paper we present a first stable numerical method to describe the wetting dynamics of liquid droplets on deformable membranes. We represent the membrane as a dimensionally reduced (hyper-) surface, which enables the accurate resolution of the high membrane curvature that is often observed as a cusp in experimental images. On the other hand, droplets are described by a phase-field model with a diffuse interface between the two liquids. This diffusive nature regularizes the stress singularity at the contact line, making phase-field models a very natural approach to describe wetting phenomena. The rigorous energy-based structure of the model allows for consistent modeling of topological transitions (e.g., [34]) and enables energy stable discrete formulations and robust time discretizations [66, 78, 5, 3].

In section 2.2, we introduce the model equations in a thermodynamically consistent way. In section 3, we present the numerical method. Benchmark tests and further illustrative simulations are carried out in section 4. Conclusions are drawn in section 5.

2. Model. We investigate an elastic, closed lipid bilayer membrane immersed in and surrounded by fluids; see Figure 2.1. The membrane is considered to have negligible thickness. The fluids undergo phase separation, resulting in two distinct phases: a condensed (droplet) phase and a dilute (ambient) phase. The interplay of surface tension and bending rigidity causes the membrane to bend.

Mathematically, the fluid domain $\Omega \in \mathrm{R}^d$ is separated by the membrane Γ into two subdomains Ω_{out} and Ω_{in}, referring to the outside and the inside of the membrane, respectively. Figure 2.1 depicts the scenario of a droplet wetting a deformable vesicle for $d = 2$. The thin membrane is represented as a hypersurface of dimension $d - 1$. An order parameter ϕ is introduced to describe the two-phase fluid, i.e., we define $\phi = 0$ in the ambient phase and $\phi = 1$ in the droplet phase. For ease of notation, we present the method for the case that phase separation occurs only on one side of the membrane. Without loss of generality, we choose Ω_{out} as the phase separating domain. The opposite case of phase separation in the interior of the membrane can

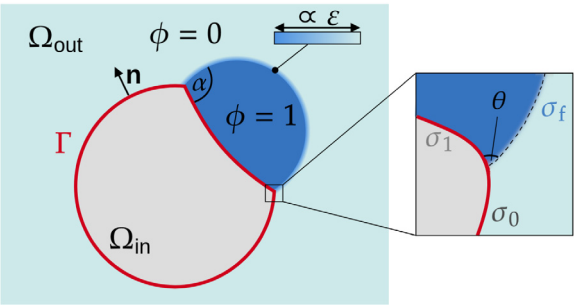

FIG. 2.1. *Illustration of a droplet wetting a vesicle. A deformable closed membrane* Γ *separates the fluid domain* Ω_{in} *and a two-phase fluid domain* Ω_{out}*. The two fluids in* Ω_{out} *are indicated by the value of the phase-field function* ϕ*. The fluid-fluid interface is diffuse with a thickness* ε *and surface tension* σ_f*. The membrane* Γ *has two distinct surface tensions* σ_0 *and* σ_1 *depending on whether it is adjacent to the dilute or the dense phase, respectively (see inset). Two different contact angles can be considered, where* α *is the macroscopic Neumann angle, that can be measured in experiments, while* θ *is the local Young's angle between the droplet interface and the locally flat membrane.*

be equivalently handled by the proposed method, as also demonstrated in the results section.

To investigate the wetting and deformation of the membrane, two different contact angles are considered in this work. The apparent contact angle α, which is generally easier to determine experimentally, is obtained by describing the membrane as having a kink at the contact point with the droplet interface. However, since the membrane has a bending rigidity, a kink at the contact point ($d = 2$) between fluid-fluid interface and membrane does not occur. Instead, the membrane is curved smoothly (see Figure 2.1, inset). This gives rise to the local contact angle θ between membrane and fluid-fluid interface at the contact point. The reaction of the membrane to bending deformations depends on the bending stiffness K_B of the membrane material, which is assumed to be constant along the membrane.

2.1. Free energy. We consider the exemplary system for droplets which are outside the membrane. The derivation for the general case of droplets being inside or on both sides of Γ is analogous. The total free energy of the system E is composed of contributions in the bulk (Ω_{out} and Ω_{in}) and on the membrane (Γ), respectively:

$$E = E_\Omega + E_\Gamma \,, \tag{2.1}$$

with

$$E_\Omega = E_{\text{kin}} + E_{\sigma_{\text{f}}} \,, \tag{2.2}$$

$$E_\Gamma = E_{\text{bend}} + E_{\sigma_{\text{m}}} + E_{\text{stretch}} \,. \tag{2.3}$$

The bulk energy E_Ω contains two contributions originating from the kinetic energy of the bulk fluid E_{kin} and from the droplet interface $E_{\sigma_{\text{f}}}$. The membrane free energy E_Γ accounts for the bending energy E_{bend}, the surface tension along the membrane, which leads to $E_{\sigma_{\text{m}}}$, and the stretching energy E_{stretch}.

The various energy contributions are tightly coupled. The fluid velocity is influenced by both the phase field and the membrane forces. Concurrently, the deformation of the membrane is affected by the velocity of the two fluids and the force response of the membrane. The membrane forces depend on the fluid in contact with the respective membrane region, i.e., they are dependent on the phase field.

We model the individual energy terms as described in the following. The kinetic energy is

$$E_{\text{kin}} = \int_\Omega \frac{\rho}{2}|\mathbf{v}|^2 \,\mathrm{d}V, \tag{2.4}$$

where ρ denotes a constant fluid density, and $\mathbf{v}$ is the hydrodynamic velocity field that is continuous across Γ. The different interfaces in the system are characterized by three distinct surface tensions. The fluid-fluid tension σ_{f} and the two membrane-fluid tensions, σ_0 and σ_1 (see Figure 2.1). Furthermore, the phase-field function ϕ has to vary smoothly across the fluid-fluid interface leading to a thin diffuse interface of width ε. The phase-field function ϕ can correspond to the concentration of molecules and the interface profile to a physical fluid-fluid interface [32, 73]. We follow [17] and write the corresponding free energy:

$$E_{\sigma_{\text{f}}} = 6\sqrt{2}\sigma_{\text{f}} \int_{\Omega_{\text{out}}} \left(\frac{\varepsilon}{2}|\nabla\phi|^2 + \frac{1}{\varepsilon}W(\phi) \right) \mathrm{d}V\,, \tag{2.5}$$

where σ_{f} is the surface tension of the interface between the droplet and the ambient liquid, and $W(\phi)$ is the bulk free energy density, for which we choose a double-well potential $W(\phi) = \frac{1}{4}\phi^2\,(1-\phi)^2$. This double-well potential is a simple model for phase transitions in mixed systems, in particular describing the phase separation in a binary mixture. The prefactor $6\sqrt{2}$ originates from our choice for $W(\phi)$ [2]. We use the abbreviation $\tilde{\sigma}_{\text{f}} = 6\sqrt{2}\sigma_{\text{f}}$ in the following.

Moreover, the bending, tension, and stretching energy for the deformable membrane are given as [21, 7]

$$E_{\text{bend}} = \int_\Gamma \frac{K_B}{2}\kappa^2 \,\mathrm{d}A\,, \tag{2.6}$$

$$E_{\sigma_{\text{m}}} = \int_\Gamma \sigma_{\text{m}}(\phi) \,\mathrm{d}A\,, \tag{2.7}$$

$$E_{\text{stretch}} = \int_\Gamma \frac{K_A}{2}\,(J-1)^2 \,\mathrm{d}A\,. \tag{2.8}$$

Here, K_B is the membrane bending stiffness and κ is the total curvature of the membrane. The surface tension $\sigma_{\text{m}}\,(\phi)$ represents the tension along Γ between the membrane and the fluid indicated by the value of the phase field. We use the following differentiable function of the phase field $\sigma_{\text{m}}\,(\phi) = (\sigma_1 - \sigma_0)\phi^2(3-2\phi) + \sigma_0$, which implies $\sigma_{\text{m}}(0) = \sigma_0$ and $\sigma_{\text{m}}(1) = \sigma_1$. For flat surfaces this choice of σ_{m} is expected to result in correct contact angles for all level sets of the phase field as observed for similar systems (e.g., [2]) and confirmed in section 2.2. Finally, K_A is the area dilation modulus and J the determinant of the deformation gradient tensor. The latter gives the local area stretch of an infinitesimal surface area segment and is equal to 1 for an undilated surface.

Remark. In three-dimensional (3D) elasticity theory, the response of an isotropic elastic body to elastic deformations can be described by two material-specific parameters: Young's modulus E and Poisson's ratio ν. For a thin elastic material of thickness d, these parameters are typically reformulated into surface parameters, for example, the area dilation modulus K_A and area shear modulus K_S and the bending modulus K_B [50]. Considering a rectangular surface element, K_A describes the response of the membrane to in-plane area changes with a constant aspect ratio of the surface

element. K_S provides information about the response to in-plane shear deformations with constant area of the surface element. However, for lipid bilayer membranes, no shear forces occur and, therefore, $K_S = 0$. The elastic surface parameters can be calculated directly from Young's modulus, Poisson ratio, and membrane thickness:

$$K_A = \frac{dE}{2(1-\nu)}, \quad K_B = \frac{d^3E}{24(1-\nu^2)}. \tag{2.9}$$

2.2. Model derivation. To derive the dynamics of the system in a thermodynamically consistent manner, we compute the time variation of the total energy (2.1). The details of these calculations can be found in the supplementary material section SM1. Assuming incompressible fluid flow ($\nabla \cdot \mathbf{v} = 0$) and constant mass density ρ, we obtain

$$\begin{aligned} d_t E = &\int_\Gamma \partial_t^\bullet \phi \left(\frac{\delta E_{\sigma_\mathrm{m}}}{\delta \phi} + \tilde{\sigma}_\mathrm{f} \varepsilon \, \mathbf{n} \cdot \nabla \phi \right) \\ &+ \mathbf{v} \cdot \left(\frac{\delta E_{\sigma_\mathrm{m}}}{\delta \Gamma} + \frac{\delta E_\mathrm{bend}}{\delta \Gamma} + \frac{\delta E_\mathrm{stretch}}{\delta \Gamma} - \tilde{\sigma}_\mathrm{f} \varepsilon \, \nabla \phi (\nabla \phi \cdot \mathbf{n}) \right) \mathrm{d}A \\ &+ \int_{\Omega_\mathrm{out}} \partial_t^\bullet \phi \frac{\delta E_{\sigma_\mathrm{f}}}{\delta \phi} + \mathbf{v} \cdot (\nabla \cdot (\tilde{\sigma}_\mathrm{f} \varepsilon \nabla \phi \otimes \nabla \phi)) \, \mathrm{d}V \\ &+ \int_{\Omega_\mathrm{in} \cup \Omega_\mathrm{out}} \rho \mathbf{v} \cdot \partial_t^\bullet \mathbf{v} \, \mathrm{d}V, \end{aligned} \tag{2.10}$$

where $\partial_t^\bullet = \partial_t + \mathbf{v} \cdot \nabla$ denotes the material time derivative and $\mathbf{n}$ denotes the normal vector of Γ pointing to Ω_out. The variational derivatives are

$$\frac{\delta E_{\sigma_\mathrm{f}}}{\delta \phi} = \tilde{\sigma}_\mathrm{f} \left(\frac{1}{\varepsilon} W'(\phi) - \varepsilon \Delta \phi \right), \tag{2.11}$$

$$\frac{\delta E_{\sigma_\mathrm{m}}}{\delta \phi} = \sigma_\mathrm{m}'(\phi), \tag{2.12}$$

$$\frac{\delta E_{\sigma_\mathrm{m}}}{\delta \Gamma} = \kappa \sigma_\mathrm{m}(\phi) \, \mathbf{n} - \nabla_\Gamma \sigma_\mathrm{m}(\phi), \tag{2.13}$$

$$\frac{\delta E_\mathrm{bend}}{\delta \Gamma} = K_B \left(\Delta_\Gamma \kappa - 2 K_g \kappa + \frac{1}{2} \kappa^3 \right) \mathbf{n}, \tag{2.14}$$

$$\frac{\delta E_\mathrm{stretch}}{\delta \Gamma} \approx K_A \kappa (J-1) \, \mathbf{n} - K_A \nabla_\Gamma (J-1). \tag{2.15}$$

The last term is a linear approximation, which is quite accurate for small stretching deformations. Since the area dilation modulus K_A is large for membranes, taking into account small stretching deformations is sufficient ($J \approx 1$). In the simulations presented in this work, J deviates from the value 1 by less than 5%. Consistent with other derivations [18, 60, 7, 72], we recover in (2.10) the capillary stress of a diffuse interface $\mathbf{S}_{\sigma_\mathrm{f}} := -\tilde{\sigma}_\mathrm{f} \varepsilon \nabla \phi \otimes \nabla \phi$. We note that our derivation considered the membrane to be impermeable, a condition which will be relaxed later to account for slow water flux through the membrane [24].

Using the usual viscous and pressure stress $\mathbf{S} = \eta(\nabla \mathbf{v} + \nabla \mathbf{v}^T) - p\mathbf{I}$, we arrive at the following evolution equations consistent with the second law of thermodynamics:

$$\partial_t \phi + \mathbf{v} \cdot \nabla \phi = M \Delta \frac{\delta E_{\sigma_\mathrm{f}}}{\delta \phi} \qquad \text{in } \Omega_\mathrm{out}\,, \tag{2.16}$$

$$\tilde{\sigma}_\mathrm{f} \varepsilon\, \mathbf{n} \cdot \nabla \phi = -\frac{\delta E_{\sigma_\mathrm{m}}}{\delta \phi} \qquad \text{on } \Gamma\,, \tag{2.17}$$

$$\mathbf{n} \cdot \nabla \frac{\delta E_{\sigma_\mathrm{f}}}{\delta \phi} = 0 \qquad \text{on } \Gamma\,, \tag{2.18}$$

$$\rho(\partial_t \mathbf{v} + \mathbf{v} \cdot \nabla \mathbf{v}) = \nabla \cdot (\mathbf{S} + \chi_\mathrm{out} \mathbf{S}_{\sigma_\mathrm{f}}) \qquad \text{in } \Omega_\mathrm{in} \cup \Omega_\mathrm{out}\,, \tag{2.19}$$

$$\nabla \cdot \mathbf{v} = 0 \qquad \text{in } \Omega_\mathrm{in} \cup \Omega_\mathrm{out}\,, \tag{2.20}$$

$$\mathbf{n} \cdot [\mathbf{S} + \chi_\mathrm{out} \mathbf{S}_{\sigma_\mathrm{f}}]_\mathrm{in}^\mathrm{out} = -\frac{\delta E_{\sigma_\mathrm{m}}}{\delta \Gamma} - \frac{\delta E_\mathrm{bend}}{\delta \Gamma} - \frac{\delta E_\mathrm{stretch}}{\delta \Gamma} \qquad \text{on } \Gamma\,. \tag{2.21}$$

Here, the M is a mobility coefficient that is considered to be constant and χ_out is the characteristic function of Ω_out, i.e., $\chi_\mathrm{out} = 1$ in Ω_out and $\chi_\mathrm{out} = 0$ in $\Omega \setminus \Omega_\mathrm{out}$. Furthermore, $[\cdot]_\mathrm{in}^\mathrm{out}$ denotes the jump of the quantity in brackets across Γ. Note that a boundary condition for velocity $\mathbf{v}$ across the membrane is not required, due to our assumption of a continuous velocity field, which implies a no-slip condition along both sides of the membrane. Note that the resulting contact angle condition (2.17) can be rewritten to $\mathbf{n} \cdot \nabla\phi/|\nabla\phi| = (\sigma_0 - \sigma_1)/\sigma_f$ using equipartition of energy E_{σ_f}. Geometrically, $\nabla\phi/|\nabla\phi|$ is the normal vector of the phase-field level sets. Hence, the above equation implies correct angles for all level sets of the phase field.

Equations (2.16)–(2.21) correspond to the incompressible Navier–Stokes equations including a capillary stress, and thereby coupled to the Cahn–Hilliard equation for the binary fluid domain, together with an interfacial balance of forces. Paired with (2.10) we obtain nonincreasing total free energy,

$$d_t E = -\int_{\Omega_\mathrm{out}} M \left| \nabla \frac{\delta E_{\sigma_\mathrm{f}}}{\delta \phi} \right|^2 \mathrm{d}V - \int_{\Omega_\mathrm{in} \cup \Omega_\mathrm{out}} \frac{\eta}{2} \|\nabla \mathbf{v} + \nabla \mathbf{v}^T\|_\mathrm{F}^2 \,\mathrm{d}V \le 0\,. \tag{2.22}$$

In summary, (2.16)–(2.21) are consistent governing equations of a membrane wetted on one side. The opposing case of wetting inside the membrane follows by interchanging the indices $()_\mathrm{in}$ and $()_\mathrm{out}$. Wetting on both sides can be handled by introducing one distinct phase field for each side of the membrane, together with a second membrane surface energy and a second capillary stress tensor.

3. Discretization.

3.1. ALE discretization. We use a fitted finite element method to discretize the system in space. The two subdomains Ω_out and Ω_in are discretized on two separate but connected, moving numerical grid partitions. An arbitrary Lagrangian-Eulerian (ALE) method is used to advect the grid with velocity $\mathbf{w}$. Thereby, in the absence of membrane permeability, grid points on Γ move with the material velocity, $\mathbf{w} = \mathbf{v}$. In contrast, the grid points in the fluids move with a continuous harmonic extension of this velocity in order to keep a proper shape of the mesh. When membrane permeability is considered, the membrane allows percolation of ambient fluid. The resulting difference between membrane and fluid normal velocity can be modeled as being proportional to the pressure difference across the membrane [62]. Consequently, the grid velocity is calculated in the two subdomains by solving the Laplace problem

$$
\begin{aligned}
\Delta \mathbf{w} &= 0 && \text{in } \Omega_{\text{in}} \cup \Omega_{\text{out}}\,, \\
\mathbf{w} &= \mathbf{v} - P\, p_{\text{diff}}\, \phi_d\, \mathbf{n} && \text{on } \Gamma\,, \\
\mathbf{w} &= 0 && \text{on } \partial\Omega/\Gamma\,.
\end{aligned} \tag{3.1}
$$

The slight membrane permeability is incorporated into the model by the term $P\, p_{\text{diff}}\, \phi_d \mathbf{n}$ from the boundary condition on Γ, with the material-specific permeability P of the membrane. For zero permeability ($P = 0$), the approach corresponds to a standard ALE method. The fact that membranes can be permeable to water on large time scales [24] can be accounted for by $P > 0$. Water flux across the membrane is driven by the pressure difference $p_{\text{diff}} = (p_{\text{out}} - p_{\text{in}}) - p_{\text{eq}}$ with the pressures p_i in Ω_i. The pressure difference p_{eq} is the equilibrium pressure difference which may result from osmotic pressure. Here, we choose p_{eq} equal to mechanical pressure jump $(p_{\text{out}} - p_{\text{in}})$ in the spherical equilibrium state. Consequently, for small droplets in two dimensions, p_{eq} is approximated by $p_{\text{eq}} = \sigma_0 / r_{\text{m}} - K_B/(2r_{\text{m}}^3)$, where r_{m} is the radius of a spherical membrane with the same volume as the present membrane. In three dimensions, the bending force of a sphere vanishes, and hence $p_{\text{eq}} = 2\sigma_0 / r_{\text{m}}$. The indicator function $\phi_d(x)$ is designed to ensure that the droplets themselves are not permeable. The permeability condition should only be imposed at a distance d away from the droplet interface to prevent instabilities caused by high pressure differences in the vicinity of the phase-field interface. This distance is dependent on the physical properties of the system (shell size, droplet number, droplet size, etc.) and can be obtained empirically. Hence, we use

$$
\phi_d(x) = \begin{cases} 1 & \text{if } x \in \Gamma \cap \{x | \phi(x) < 0.5\} \cap \left\{ x \middle| \min_{x_{0.5} \in \Gamma_{0.5}} \|x - x_{0.5}\| > d \right\}, \\ 0 & \text{else,} \end{cases} \tag{3.2}
$$

where $\Gamma_{0.5} = \Gamma \cap \{x | \phi(x) = 0.5\}$. Further, a typical value for d is 3ε.

Finally, the calculated grid velocity $\mathbf{w}$ is subtracted in all convective terms of the governing equations. Therefore, the material derivate $\partial_t^\bullet$ is replaced by

$$
\partial_t^\bullet \to \partial_{t,x^*} + (\mathbf{v} - \mathbf{w}) \cdot \nabla\,, \tag{3.3}
$$

where ∂_{t,x^*} defines the time derivative of a quantity along a moving grid point.

Remark. The ad hoc introduction of permeability interferes with the thermodynamic consistency of the system. In particular, the energy change in (2.22) is augmented by an additional contribution of the flux of Cahn–Hilliard energy density through the membrane. Our approach to allow permeation only away from the phase-field interface (through ϕ_d) minimizes this effect, but cannot eliminate it completely. Moreover, since the permeability itself is slow compared to the dynamics of the membrane due to membrane/surface tensions and bending stiffness, the violation of thermodynamic consistency is expected to be negligible in practice.

3.2. Time discretization. The problem is discretized with equidistant time steps of size τ. At each time step, the general workflow of the numerical solution procedure is as follows. First, the coupled system of momentum balance, mass balance, and phase-field evolution, (2.16)–(2.21), is solved in one monolithic system. Afterward the grid velocity $\mathbf{w}$ is computed as explained in section 3.1. Then in a last step, the grid is updated, that is, each grid point is moved by the corresponding value of $\mathbf{w}$. An IMEX (implicit/explicit) Euler method is used to formulate a time discretization of (2.16)–(2.21), which is linear in the solution variables. We denote quantities on

discrete time points by a superscript, where $()^{n-1}$ refers to the previous time step and $()^n$ refers to the current time step. In order to compute bending, stretching, and surface tension forces, we compute the curvature vector $\varkappa = -\kappa \boldsymbol{n}$ for the current time step as a solution variable of the system, where we use the fact that $\Delta_\Gamma \mathrm{id}_\Gamma = -\kappa \mathbf{n}$ with id_Γ the identity map on Γ. This way, the stability of the system is increased by an implicit treatment of all membrane forces.

The capillary stress $\boldsymbol{S}_{\sigma_\mathrm{f}}$ is taken semi-implicitly by using $\tilde{\sigma}_\mathrm{f}\varepsilon \nabla\phi^n \otimes \nabla\phi^{n-1}$. Note that we define the involved tensor product such that

$$\nabla \cdot \left(\nabla\phi^n \otimes \nabla\phi^{n-1}\right)_i = \sum_j \partial_j \left(\partial_j \phi^n \partial_i \phi^{n-1}\right).$$

This treatment must be accompanied by using the new velocity field $\mathbf{v}^n$ in the advective term of the phase field. Further, the nonlinear derivative of the double well potential $W'(\phi)$ is linearized by a first order Taylor expansion. We end up with the following time discrete system:

In each time step n, find $\mathbf{v}^n$, p^n_out, p^n_in, ϕ^n, $\mu^n, \varkappa^n, \mathbf{f}^n_\Gamma$ such that

$$\left.\begin{aligned} \overline{\rho}^{n-1}\left(\frac{\mathbf{v}^n - \mathbf{v}^{n-1}}{\tau} + \left(\mathbf{v}^{n-1} - \mathbf{w}^{n-1}\right)\cdot\nabla\mathbf{v}^n\right) \\ = -\nabla\left(\chi^{n-1}_\mathrm{out} p^n_\mathrm{out} + \chi^{n-1}_\mathrm{in} p^n_\mathrm{in}\right) + \nabla\cdot\left(\overline{\eta}^{n-1}\left(\nabla\mathbf{v}^n + (\nabla\mathbf{v}^n)^T\right)\right) \\ -\nabla\cdot\left(\chi^{n-1}_\mathrm{out}\tilde{\sigma}_\mathrm{f}\varepsilon\nabla\phi^n\otimes\nabla\phi^{n-1}\right) - \delta^{n-1}_\Gamma \mathbf{f}^n_\Gamma \\ \nabla\cdot\mathbf{v}^n = 0 \end{aligned}\right\} \quad \text{in } \Omega^{n-1}, \tag{3.4}$$

$$\left.\begin{aligned} \left(\frac{\phi^n - \phi^{n-1}}{\tau} + \mathbf{v}^n\cdot\nabla\phi^{n-1} - \mathbf{w}^{n-1}\cdot\nabla\phi^n\right) = M\Delta\mu^n \\ \mu^n = \tilde{\sigma}_\mathrm{f}\varepsilon^{-1}\left(W'\left(\phi^{n-1}\right) + W''\left(\phi^{n-1}\right)\left(\phi^n - \phi^{n-1}\right)\right) + \tilde{\sigma}_\mathrm{f}\varepsilon\Delta\phi^n \end{aligned}\right\} \quad \text{in } \Omega^{n-1}_\mathrm{out}, \tag{3.5}$$

(3.6)

$$\left.\begin{aligned} \mathrm{id}^n_\Gamma = \tau\left(\mathbf{v}^n - P\, p^{n-1}_\mathrm{diff}\,\phi_d^{n-1}\mathbf{n}^{n-1}\right) + \mathrm{id}^{n-1}_\Gamma \\ \varkappa^n = \Delta_\Gamma \mathrm{id}^n_\Gamma \\ \mathbf{f}^n_\Gamma = \sigma_\mathrm{m}(\phi^{n-1})\varkappa^n + \sigma'_\mathrm{m}(\phi^{n-1})\nabla_\Gamma\phi^n - \left(\frac{\delta E_\mathrm{bend}}{\delta\Gamma}\right)^{n-\frac{1}{2}} - \left(\frac{\delta E_\mathrm{stretch}}{\delta\Gamma}\right)^{n-\frac{1}{2}} \end{aligned}\right\} \quad \text{on } \Gamma.$$

Here, $\mu = \frac{\delta E_{\sigma_\mathrm{f}}}{\delta\phi}$ denotes the chemical potential, and the superscript $^{n-1}$ denotes the corresponding quantities from the last time step, but after the applied change of the grid point coordinates due to the mesh update. The bending force $(\frac{\delta E_\mathrm{bend}}{\delta\Gamma})^{n-\frac{1}{2}}$ is computed with a semi-implicit scheme which will be described in section 3.3.3, where linear occurrences of the curvature vector $\varkappa$ are taken from the current time step. The stretching force $(\frac{\delta E_\mathrm{stretch}}{\delta\Gamma})^{n-\frac{1}{2}}$ mainly depends on the curvature vector and the deformation gradient determinant J, which can be seen as the local membrane area change A/A_0. An implicit prediction of J is crucial to eliminate the numerical stiffness of the coupling between shape evolution and hydrodynamics. As a consequence from the Reynolds transport theorem on surfaces, J follows the evolution

$$\partial_t J + \mathbf{w}\cdot\nabla J = J\nabla_\Gamma\cdot\mathbf{w} \qquad \text{on } \Gamma, \tag{3.7}$$

where we recall that $\mathbf{w}_{|\Gamma}$ is the membrane velocity. Assuming that membrane permeability is slow compared to the dynamics stemming from surface tension and bending

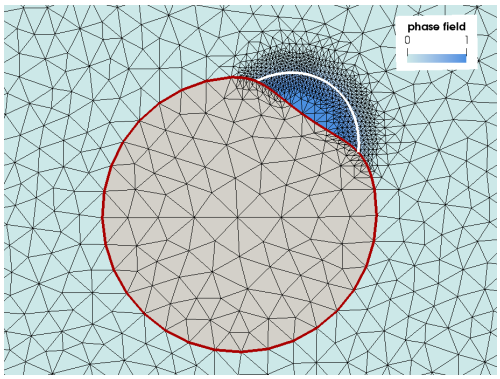

FIG. 3.1. *Illustration of the numerical mesh. The membrane triangulation T_Γ (red) is fitted to the triangulations T_{in} (gray) and T_{out}. The phase field ϕ representing the droplet is defined in T_{out} and controls the adaptive refinement. The white line indicates the fluid-fluid interface as 0.5-level set of ϕ.*

stiffness, we approximate the right-hand side by $J\nabla_\Gamma \cdot \mathbf{v}$. Thus, an implicit prediction of J^n is given by updating the current value J^{n-1} according to

$$J^n = J^{n-1} + \tau J^{n-1} \nabla_\Gamma \cdot \mathbf{v}^n \,, \tag{3.8}$$

where J^{n-1} is computed from current coordinates of the surface grid. Note that the convective term in (3.7) is no longer necessary as J^{n-1} is computed after the grid movement with velocity $\mathbf{w}$. The viscosity $\overline{\eta}$ depends on the subdomain and on the phase field, i.e.,

$$\overline{\eta} = \begin{cases} \eta_{\text{in}} & \text{in } \Omega_{\text{in}}, \\ \eta_{\text{out}}(\phi) = \eta_{\text{out},1}\phi + \eta_{\text{out},0}(1-\phi) & \text{in } \Omega_{\text{out}}, \end{cases} \tag{3.9}$$

where η_{in}, $\eta_{\text{out},0}$, and $\eta_{\text{out},1}$ are prescribed constants. The density $\overline{\rho}$ is chosen here to be constant in all fluid phases. Considering variable densities formally requires additional force terms for thermodynamic consistency (see [1]). However, the effects of this would not be noticable in practice, as biomembrane wetting interactions typically happen at Reynolds numbers $< 10^{-6}$, where density variations don't matter.

3.3. Space discretization. In our finite element approach, we consider the triangulations T_{out} of Ω_{out} and T_{in} of Ω_{in}, whereby the membrane Γ, which connects the two domains, is triangulated by $T_\Gamma = T_{\text{out}} \cap T_{\text{in}}$. In particular, the connection is ensured by the fact that every grid point on the interface of Ω_{out} is also a grid point on the interface of Ω_{in}. This fitted grid approach allows us to exactly enforce continuity of velocity across Γ. The jump conditions of the stress are implemented by definition of separate finite element spaces for T_{out} and T_{in}, such that each degree of freedom on the membrane T_Γ exists twice—one belonging to T_{out} and one belonging to T_{in}. An example for the numerical mesh is shown in Figure 3.1.

We now present the combined discrete system of (2.16)–(2.21) in the weak form. Adopting the approach from [49], we introduce the following finite element spaces:

$$
\begin{aligned}
V_h &:= \left\{ v \in C^0(\overline{\Omega}) \,|\, v_{|k} \in P_2(k), k \in T_{\text{out}} \cup T_{\text{in}} \right\}, \\
P_{h,i} &:= \left\{ q \in C^0(\overline{\Omega}_i) \,|\, q_{|k} \in P_1(k), k \in T_i \right\}, \quad i = \text{out, in}, \\
C_h &:= \left\{ c \in C^0(\overline{\Omega}_{\text{out}}) \,|\, c_{|k} \in P_2(k), k \in T_{\text{out}} \right\}, \\
S_h &:= \left\{ f \in C^0(\Gamma), |\, f_{|k} \in P_1(k), k \in T_\Gamma \right\}.
\end{aligned} \tag{3.10}
$$

Here, V_h is the finite element space for the components of the velocity $\mathbf{v}$. It ensures continuity of the respective variables across T_Γ. Note that in (3.10), i denotes a placeholder for the distinction between the two fluid domains. The use of two separate spaces, $P_{h,\text{out}}$ and $P_{h,\text{in}}$, is motivated by the discontinuity of pressure across Γ caused by the closed elastic membrane. The use of standard finite element spaces for the discretization of the discontinuous pressure leads to poor numerical properties, with an approximation order of only $\mathcal{O}(\sqrt{h})$ w.r.t. to the L^2 norm [28]. Accordingly, the usage of two separate spaces, $P_{h,\text{out}}$ and $P_{h,\text{in}}$, extends the standard Taylor–Hood finite element space by additional degrees of freedom of the pressure at the interface, such that the discontinuity can be exactly resolved. The finite element space C_h refers to ϕ and μ in (3.5). The remaining finite element space S_h is used to compute the force exerted by the elasticity of the membrane, namely surface tension, in-plane stretching, and bending stiffness.

While all equations are addressed within a unified coupled system, we opt to present them individually in the following, segregated into fluid motion, phase separation, and membrane forces, to enhance readability.

3.3.1. Navier–Stokes system. With the previous arguments, we can establish a uniform weak formulation of the momentum and mass conservation equation for the combined domain Ω. The weak form reads as follows:

Find $(\mathbf{v}^n, p^n_{\text{out}}, p^n_{\text{in}}) \in V_h^d \times P_{h,\text{out}} \times P_{h,\text{in}}$ such that $\forall (\mathbf{z}, q_{\text{out}}, q_{\text{in}}) \in V_h^d \times P_{h,\text{out}} \times P_{h,\text{in}}$,

$$
\begin{aligned}
0 = & \int_{\Omega^{n-1}} \rho \left(\frac{\mathbf{v}^n - \mathbf{v}^{n-1}}{\tau} + \left(\mathbf{v}^{n-1} - \mathbf{w}^{n-1} \right) \cdot \nabla \mathbf{v}^n \right) \cdot \mathbf{z} \\
& \quad + \left(\overline{\eta}^{n-1} \left(\nabla \mathbf{v}^n + (\nabla \mathbf{v}^n)^T \right) \right) : \nabla \mathbf{z} \, \mathrm{d}V \\
& - \int_{\Omega^{n-1}_{\text{out}}} \tilde{\sigma}_{\mathrm{f}^\varepsilon} \nabla \phi^n \otimes \nabla \phi^{n-1} : \nabla \mathbf{z} + p^n_{\text{out}} \nabla \cdot \mathbf{z} \, \mathrm{d}V \\
& - \int_{\Omega^{n-1}_{\text{in}}} p^n_{\text{in}} \nabla \cdot \mathbf{z} \, \mathrm{d}V \\
& - \int_{\Gamma^{n-1}} \mathbf{f}^n_\Gamma \cdot \mathbf{z} \, \mathrm{d}A,
\end{aligned} \tag{3.11}
$$

$$
0 = \int_{\Omega^{n-1}_{\text{out}}} q_{\text{out}} \nabla \cdot \mathbf{v}^n \, \mathrm{d}V + \int_{\Omega^{n-1}_{\text{in}}} q_{\text{in}} \nabla \cdot \mathbf{v}^n \, \mathrm{d}V . \tag{3.12}
$$

3.3.2. Cahn–Hilliard system. The weak form of (3.5) equipped with boundary conditions (2.17)–(2.18) reads as follows:

Find $(\phi^n, \mu^n) \in C_h \times C_h$ such that $\forall (\psi_1, \psi_2) \in C_h \times C_h$,

$$
0 = \int_{\Omega^{n-1}_{\text{out}}} \left(\frac{\phi^n - \phi^{n-1}}{\tau} + \mathbf{v}^n \cdot \nabla \phi^{n-1} - \mathbf{w}^{n-1} \cdot \nabla \phi^n \right) \psi_1 + M \nabla \mu^n \cdot \nabla \psi_1 \, \mathrm{d}V, \tag{3.13}
$$

(3.14)
$$0 = \int_{\Omega_{\text{out}}^{n-1}} \mu^n \psi_2 - \tilde{\sigma}_{\text{f}} \varepsilon \nabla \phi^n \cdot \nabla \psi_2 - \frac{\tilde{\sigma}_{\text{f}}}{\varepsilon} \left(W'\left(\phi^{n-1}\right) + W''\left(\phi^{n-1}\right)\left(\phi^n - \phi^{n-1}\right)\right) \psi_2 \, \mathrm{d}V - \int_{\Gamma^{n-1}} \sigma'_{\text{m}}(\phi^{n-1}) \psi_2 \, \mathrm{d}A \,.$$

Let us note that the Cahn–Hilliard system is still directly coupled to the Navier–Stokes system by the presence of $\mathbf{v}^n$ in (3.13) and the presence of ϕ^n in (3.11). This coupling removes time step restrictions for small interface thickness [3].

3.3.3. Membrane force system. The bending force (2.14) includes the total surface curvature and its derivatives. In order to formulate a stable discretization, these terms need to be included implicitly to the system. Therefore, we use the weak formulation from Dziuk [21]:

$$\int_\Gamma \frac{\delta E_{\text{bend}}}{\delta \Gamma} \boldsymbol{\psi} = K_B \int_\Gamma \frac{1}{2} |\varkappa|^2 \nabla_\Gamma \cdot \boldsymbol{\psi} + \nabla_\Gamma \varkappa : \nabla_\Gamma \boldsymbol{\psi} + \nabla_\Gamma \cdot \varkappa \nabla_\Gamma \cdot \boldsymbol{\psi} - \left(\nabla_\Gamma \boldsymbol{\psi} + \nabla_\Gamma \boldsymbol{\psi}^T \right) \mathbf{P} : \nabla_\Gamma \varkappa \, \mathrm{d}A \tag{3.15}$$

for any vector valued test function $\boldsymbol{\psi}$. Derivations can be found in [21, 12]. However, we also derived (3.15) in the present notation in the supplementary material section SM2. The resulting weak form of the combined membrane force system reads as follows:

Find $(\varkappa^n, \mathbf{f}_\Gamma^n) \in S_h^d \times S_h^d$, such that $\forall (\mathbf{s}_1, \mathbf{s}_2) \in S_h^d \times S_h^d$,

(3.16)
$$0 = \int_{\Gamma^{n-1}} \varkappa^n \cdot \mathbf{s}_1 + \nabla_\Gamma \left(\mathrm{id}_\Gamma^{n-1} + \tau \mathbf{v}^n \right) : \nabla_\Gamma \mathbf{s}_1 \, \mathrm{d}A \,,$$

$$0 = \int_{\Gamma^{n-1}} \mathbf{f}_\Gamma^n \cdot \mathbf{s}_2 - \left(\sigma_{\text{m}}(\phi^{n-1}) \varkappa^n + \sigma'_{\text{m}}(\phi^{n-1}) \nabla_\Gamma \phi^n \right) \cdot \mathbf{s}_2 - K_B \Big[- \frac{1}{2} \left(\varkappa^n \cdot \varkappa^{n-1} \nabla_\Gamma \cdot \mathbf{s}_2 \right) - \nabla_\Gamma \varkappa^n : \nabla_\Gamma \mathbf{s}_2 - \nabla_\Gamma \cdot \varkappa^n \nabla_\Gamma \cdot \mathbf{s}_2 + \left(\nabla_\Gamma \mathbf{s}_2 + \nabla_\Gamma \mathbf{s}_2^T \right) \mathbf{P}^{n-1} : \nabla_\Gamma \varkappa^n \Big]$$

(3.17)
$$- K_A \left[(J^n - 1) \varkappa^{n-1} \cdot \mathbf{s}_2 + \nabla_\Gamma (J^n - 1) \cdot \mathbf{s}_2 \right] \, \mathrm{d}A \,.$$

Note that the resulting force $\mathbf{f}_\Gamma^n$ is as well directly coupled to the Navier–Stokes–Cahn–Hilliard system by the presence of $\mathbf{v}^n$ in (3.16) and ϕ^n in (3.17). The force itself is plugged into the Navier–Stokes system in (3.11). As the discrete system is linear, (3.11)–(3.17) can be monolithically assembled and no subiterations are needed.

3.4. Remeshing. While the grid update method outlined in section 3.1 is well-suited for minor deformations of the membrane, it encounters challenges when substantial membrane deformations occur. Particularly in the proximity of the contact region between the droplet and the membrane, elements may be pushed toward each other, resulting in distorted triangles/tetrahedra with small minimum angles, undermining accuracy and stability of the finite element method. Consequently, we use a mechanism to reconstruct the mesh whenever the minimum angle of any triangle falls below a specified threshold α_{min} (in the simulations, α_{min} has been chosen between 5° and 10°). The following retriangulation steps are performed:

1. Extract the membrane grid points. Note that the adaptively refined grid has to be used here in order to retain accurate information on the membrane shape.

2. Generate a new (unrefined) mesh with `gmsh` [25], using the outer boundary box and the membrane grid points from the old grid.
3. Interpolate the data of the solution ϕ and the deformation gradient determinant J to the new grid (see the step below). J is needed to preserve the information of the unstretched initial state of the membrane. Refine the grid afterward by refinement of all elements that are on the fluid-droplet interface (i.e., where values of ϕ are between 0.05 and 0.95). Repeat the step until the refinement level of the old grid is reached. Always exclude elements from the refinement, which have a size smaller than a prescribed minimum (typically in the order of the average element volume on the interface of the old grid). This has to be done since for the new unrefined grid, grid points on the membrane from the old refined grid have been used.
4. Interpolate the data of the solution $\mathbf{v}$ by solution of the following problem, which ensures that the velocity remains divergence-free on the new grid:

$$\mathbf{v}_{\text{new}} - \nabla L = \mathbf{v}_{\text{old}}\,,$$
$$\nabla \cdot \mathbf{v}_{\text{new}} = 0\,,$$

   where L acts as a Lagrange multiplier. The problem is solved with finite elements on the new grid. However, the right- hand-side operator in the weak form is of the form $\int_{T_{\text{new}}} \mathbf{v}_{\text{old}} \cdot \boldsymbol{\psi}$ with the triangulation T_{new} based on the new grid and test functions $\boldsymbol{\psi}$ defined on the new grid. In contrast, the ansatz functions are defined on the old grid. Computation of such an integral involves identifying all intersections that an element on the new grid has with the old grid. These intersections are then triangulated, and this triangulation is utilized to calculate the integral on the respective element on T_{new}. In the implementation, this process is carried out within the `dune` module `dune-grid-glue`. Further details can be found in [14].
5. Update all data structures to the new grid and solve the next time step with the old solutions from step 4.

4. Numerical tests. We perform numerical tests to validate the proposed method and to illustrate its potential. The majority of the physical parameters are selected within the realm of realistic biological systems (see Table 4.1). Although some parameters are well-established, others, such as viscosity and surface tension of condensates, can exhibit significant variability, with observed ranges spanning four orders of magnitude. Given that the aim of this paper is not to concentrate on a particular biological system, we intentionally vary parameters across a broad spectrum. Despite the numerical method's capability to handle phase-dependent viscosity [8], we choose constant viscosity throughout this work for simplicity.

4.1. Validation. To validate the numerical method, we consider membrane remodeling induced by a single droplet in two dimensions. Assuming an initially flat membrane sheet, which is significantly larger than the droplet, enables the analytical derivation of the stationary morphology based on shape equations (see the supplementary material section SM3). To compare with these analytical shapes, we set up the numerical method to simulate the evolution up to the stationary state. The membrane ends are connected to the boundary of the domain with a free-slip condition. Membrane stretching and permeability are neglected ($K_A = P = 0$).

Figure 4.1 shows the comparison of stationary shapes between numerical and analytical results. The given local contact angle θ is related to the surface tensions through the Young–Dupré law,

TABLE 4.1
Characteristic parameters of membrane vesicles and biomolecular coacervates.

Parameter name	Value	Reference
bending rigidity K_B	$10^{-19} - 10^{-18}\,Nm$	[22, 40]
surface tension coacervate σ_f	$10^{-4} - 1\,mN/m$	[74]
viscosity η		
cytosol	$1 - 10\,Pa\,s$	[75]
coacervate	$0.1 - 10^3\,Pa\,s$	[74]
interface width ϵ	$5 - 10\,nm$	[71]
cytosol density ρ	$\sim 10^3\,kg/m^3$	[53]
area dilation modulus K_A	$100 - 300\,mN/m$	[23, 58]
scaled permeability Pp_{diff}	$10^{-7} - 10^{-5}\,m/s$	[55, 63]

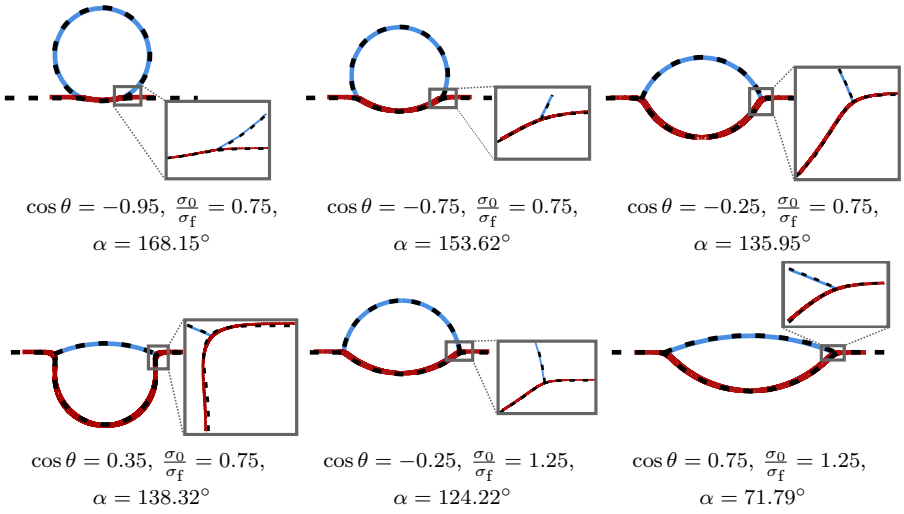

FIG. 4.1. *Comparison of stationary shapes obtained by simulations (dashed lines) and theoretical model (solid lines) for a single droplet (blue) on an initially flat membrane (red). Compelling agreement between the two solutions is even visible in the close-up around the three-phase contact point. Parameters: Initial droplet shape is spherical (radius* $50nm$*) in the theoretical model, and half-spherical cap (radius* $70.71nm$*) in the simulations. The used surface tensions can be determined from* (4.1) *with* $\sigma_f = 15\mu N/m$*. Further,* $K_A = 0, K_B = 8 \cdot 10^{-20} Nm$*,* $P = 0$ $\varepsilon = 1nm$*.*

$$\cos\theta = \frac{\sigma_0 - \sigma_1}{\sigma_\mathrm{f}}, \tag{4.1}$$

and differs from the apparent contact angle α (see Figure 2.1), which in the limit of both large droplets (compared to the capillarity length) and large vesicles (compared to the droplet) is given by Neumann's law [36]:

$$\cos\alpha = \frac{\sigma_0^2 - \sigma_1^2 - \sigma_\mathrm{f}^2}{2\sigma_\mathrm{f}\sigma_1}. \tag{4.2}$$

The surface tensions have been chosen such that different resulting shapes can be compared, from a nearly spherical droplet with very low bending of the membrane, Figure 4.1(a), over strong indentation of the membrane by the droplet, Figure 4.1(d), to a lens-like shape of the droplet on the membrane Figure 4.1(f). For all different parameter configurations chosen, we observe a perfect agreement between numerical results and the results of the shape equations. This verifies that the numerical method

TABLE 4.2

Experimental order of convergence (EOC) in space for a 2D test simulation with an initially half spherical droplet (radius 1.5 μm) on a spherical membrane (radius 5 μm). The meshes for the three test cases are illustrated in Figure 4.2. Here, $\mathbf{x}^* = (x^*, 0)^T$ is the right membrane point on the x-axis. All values are evaluated at the 10th time step. Parameters: $\varepsilon = 0.02\mu m$, $K_B = 8 \cdot 10^{-20}\, Nm$, $K_A = 5 \cdot 10^{-3}\ N/m$, $P = 10^{-8} m^2 s/kg$, $\eta = 10\, Pa \cdot s$, $\rho = 10^3\, kg/m^3$.

Benchmark		**Grid size**		**EOC**
Quantity	h	$h/2$	$h/4$	
x^*	0.490525	0.490670	0.490716	1.66
$\int_{\{\phi=0.5\}} 1\, dA$	0.5065	0.5022	0.5018	3.43
$\int_\Gamma \|\varkappa\|_2\, dA$	9.69082	7.98518	7.62019	2.22

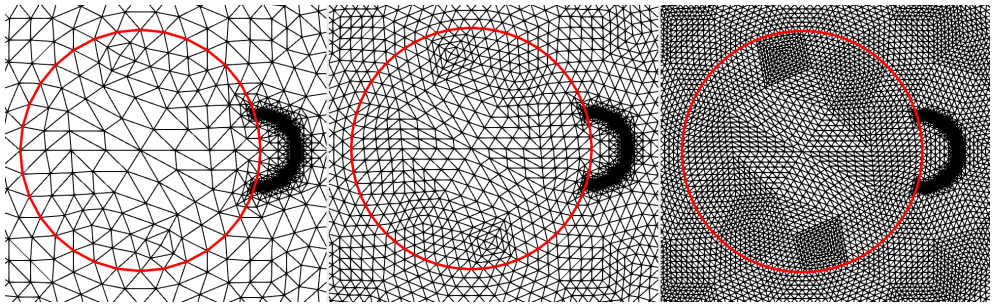

FIG. 4.2. *Meshes for the convergence test at initial state. The same base mesh (left, mesh size h) is refined once (center, mesh size h/2) and twice (right, mesh size h/4), by splitting each base triangle into four subtriangles. On the membrane, refinement is done such that it is still circular after refinement, i.e., all membrane grid points have a distance of 5 μm to the origin. While the described refinement is performed globally before creation of the phase field, the images show the meshes after adaptive refinement at the phase-field interface.*

accurately incorporates all surface forces and resolves the locally high membrane curvature in the triple contact point by the adaptive grid.

The hydrodynamics of the numerical method and the underlying flow solver have been previously validated in various two-phase applications on cells and shells in fluid flow [51, 19]. Furthermore, benchmark validations against other numerical codes [8], experimental data [4, 3], and convergence studies [8, 49] have been successfully conducted. Moreover, the wetting boundary conditions were validated for dynamic situations and applied to scenarios of moving contact lines [48]. To assess the spatial accuracy of the full droplet/membrane interaction, we conduct a very brief study in Table 4.2 and find roughly second to third order convergence for different geometric quantities.

Consequently, the method exhibits precise capabilities in capturing dynamic phenomena, making it well-suited for application in future studies leveraging realistic experimental data.

4.2. Droplets on a vesicle. This section aims to showcase the outcomes of numerical investigations involving droplets adhering to an initially spherical membrane. We start with single droplets on the membrane. Afterward, multiple droplets on the membrane are considered. To begin, we examine the interaction dynamics of two closely positioned droplets and explore how the bending stiffness of the membrane influences the interplay between these two droplets. Finally, we consider liquid-liquid phase separation around the membrane with condensates of low, neutral, and high

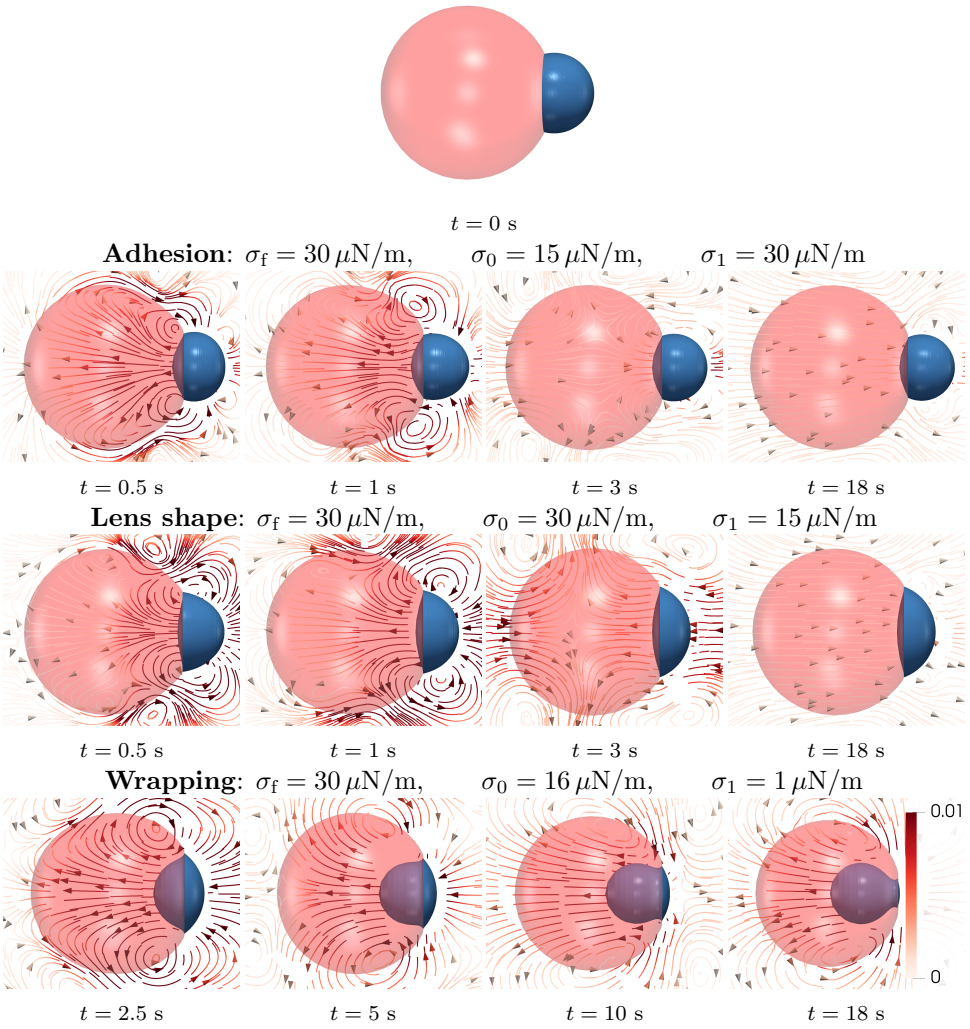

FIG. 4.3. *Time evolution for three different parameter configurations exhibit different categories of droplet-membrane interaction: adhesion (top row), lens shape (middle row), and wrapped/endocytosis (bottom row). The single top snapshot shows the initial configuration of droplet (blue) and membrane (red). Oriented streamlines illustrate fluid velocity in the xy-plane colored by magnitude in units of* $10\,\mu m/s$. *All snapshots have been zoomed in for visibility and therefore do not show all of* Ω. *Parameters: Initially spherical membrane of radius of* $5.4\mu m$ *and half-spherical cap droplet of radius* $2.5\mu m$, *centered on the membrane. Other parameters are* $\varepsilon = 0.02\mu m$, $K_B = 8 \cdot 10^{-19}\,Nm$, $K_A = 5 \cdot 10^{-3}\ N/m$, $P = 10^{-7} m^2 s/kg$, $\eta = 1\,Pa \cdot s$, $\rho = 10^3\,kg/m^3$. *Axisymmetric simulations.*

wettability, respectively. These simulations illustrate the capabilities of the present model.

4.2.1. Single droplet. In the following we consider a single droplet situated outside a spherical vesicle membrane. Three distinct combinations of surface tensions were selected to explore shape evolutions into different categories of stationary states, as introduced in [45]: adhesion, lens shape, and partially wrapped/endocytosis.

Case 1: Adhesion (Figure 4.3, top row). Here σ_0 is chosen smaller than the other two tensions. As a result, the droplet indents the membrane slightly. During

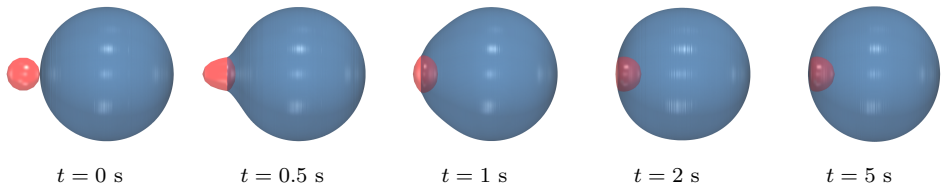

FIG. 4.4. *Inverted endocytosis: A small spherical vesicle (red) is absorbed by a larger drop (blue). Time evolution of axisymmetric simulation. Vesicle can change shape due to imposed permeability. Parameters:* $\sigma_f = 30\,\mu N/m$, $\sigma_0 = 31\,\mu N/m$, $\sigma_1 = 1\,\mu N/m, K_B = 8 \cdot 10^{-17}\,Nm, K_A = 5 \cdot 10^{-3}\,N/m, P = 10^{-7} m^2 s/kg$, *initial radii* $1.25\,\mu m$ *(vesicle),* $5\,\mu m$ *(drop). Axisymmetric simulation.*

the indentation, all three fluids (droplet, ambient, intramembrane) are set in motion. This motion decays as the system reaches a (nearly) stationary state around $t = 18$s. The observed contact angle of approximately $\alpha = 135°$ is lower than the theoretical prediction of 151° from (4.2). This is due to the fact that droplet and membrane radius are of the same order of magnitude, hence, Neumann's law does not hold.

Case 2: Lens shape (Figure 4.3, middle row). In the lens shape case, σ_1 is smaller than the other two surface tensions. Hence, the droplet tends to cover more of the membrane's surface, leading to a smaller contact angle ($\theta \approx 85°$) and the lens-like shape of the droplet in the stationary state.

Case 3: Wrapping (Figure 4.3, bottom row). For this test case, the values of the surface tensions are chosen such that the capillary forces of the droplet are dominant and there is a minimum influence of the membrane tension at the contact surface between droplet and membrane. The droplet sinks completely into the membrane and gets wrapped by it. Since the present ALE model is not able to describe topological changes of the membrane, the simulations were stopped at $t = 18$ s before a stationary state was reached. As predicted by theory [45], the droplet should be completely wrapped such that endocytosis happens. In this case, it is clearly observable that the volume enclosed by the membrane decreases as the droplet sinks into it. This effect occurs due to the interplay between in-plane elasticity (high K_A) and membrane permeability. The increase of membrane area which is necessary to wrap the droplet is opposed by the dilational elasticity, leading to a high pressure inside the membrane, pushing out fluid such that its volume decreases.

Inverted endocytosis. An opposite case of inverted endocytosis is illustrated in Figure 4.4. Here, a small vesicle is absorbed into a larger droplet, driven by surface tension forces. The surface tensions are chosen such that the extreme case of a contact angle of $\theta = 0°$ is approached. In this case, the full endocytosis can be simulated, since the topological transition happens now for the *diffuse* fluid-fluid interface instead of the membrane.

4.2.2. Multiple droplets. Another interesting test scenario is the inverted Cheerios effect. This effect, which has been reported experimentally [33] and numerically [7], describes the mutual attraction or repulsion of droplets, mediated by elasticity of their underlying substrate. Here, we perform simulations in two dimensions with an initially spherical membrane, where the two drops are represented as spherical caps, placed outside the membrane with a small distance in between. An illustration of the resulting dynamics is depicted in Figure 4.5 for two different values of bending stiffness. Other parameters are chosen equal to the previous lens shape case. Accordingly, at early times we observe a similar evolution for the two droplets as

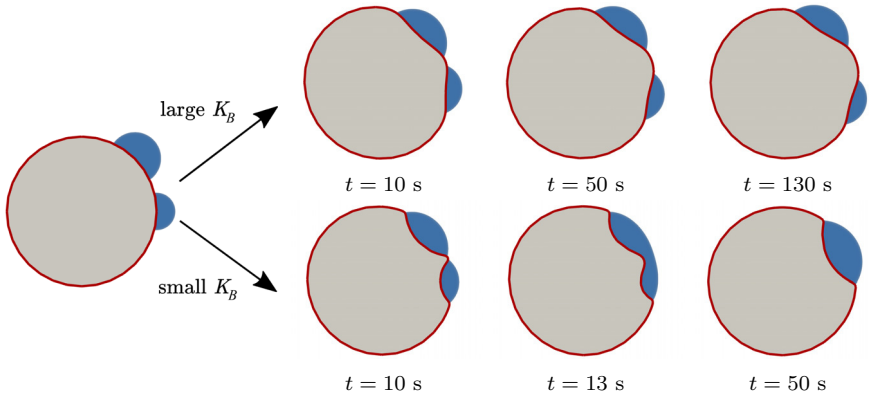

FIG. 4.5. *Inverted Cheerios effect: Droplets repel each other mediated by membrane bending (top, $K_B = 8 \cdot 10^{-17}$ Nm). For low bending stiffness, the effect is not present and droplets coalesce (bottom, $K_B = 8 \cdot 10^{-19}$ Nm). Parameters: Initial membrane radius $10\,\mu$m. Two droplets are placed as spherical caps with radius $r_1 = 2.5\,\mu$m and $r_2 = 3.5\,\mu$m at the membrane, where the centers of the two drops are $c_1 = (10, 0)^T$ and $c_1 = (7.1, 7.1)^T$. The remaining parameters have been chosen equal to the lens shape case of the single droplet simulations.*

before, Figure 4.5. The droplets indent the membrane until the forces on the membrane due to bending stiffness and surface tension are (nearly) in equilibrium around $t = 10$ s. However, in the case of larger bending stiffness, the droplets are driven apart from each other due to the high membrane curvature between the droplets, Figure 4.5 (top row). This membrane-mediated droplet repulsion happens on a much slower time scale than the initial indentation of the membrane. Contrarily, in the case of smaller bending stiffness, Figure 4.5 (bottom row), the distance between the two droplets decreases until both droplets merge and, as a result, the stationary shape is a single lens shaped droplet comparable to that in Figure 4.3.

4.2.3. Phase separation around a membrane. Finally, we investigate phase separation around a membrane. We study three different situations, namely phase separation on the inside, on the outside, and on both sides of a vesicle. For each of these cases, three different parameter configurations are studied: neutral ($\theta = 90°$), high wettability ($\theta = 60°$), and low wettability ($\theta = 120°$).

In order to simulate phase separation, the phase field was initialized with random values around the membrane ($\phi \in [0.2, 0.3]$ uniformly). An illustration of the resulting dynamics is shown in Figure 4.6 (neutral), Figure 4.7 (high wettability), and Figure 4.8 (low wettability). In the neutral case ($\theta = 90°$), numerous small droplets initially appear in the proximity of the membrane at $t = 0.5$ s. Subsequently, these droplets undergo growth by coalescence and Ostwald ripening. During this process, the membrane morphology increasingly adjusts, since larger droplets induce stronger deformations.

In the cases of high and low wettability (Figures 4.7, 4.8), we initialize the order parameter with larger values ($\phi \in [0.2, 0.8]$ uniformly) such that larger droplets emerge. Consequently, we observe enhanced membrane remodeling, accompanied by strong fluid motion. For high wettability ($\theta = 60°$) the rich dynamics also enable the emergence of transient droplets of the ambient fluid. Membrane remodeling generally seems to assist the coarsening and merging of droplets, such that only a few droplets remain at final time. However, when condensate is present on both sides of

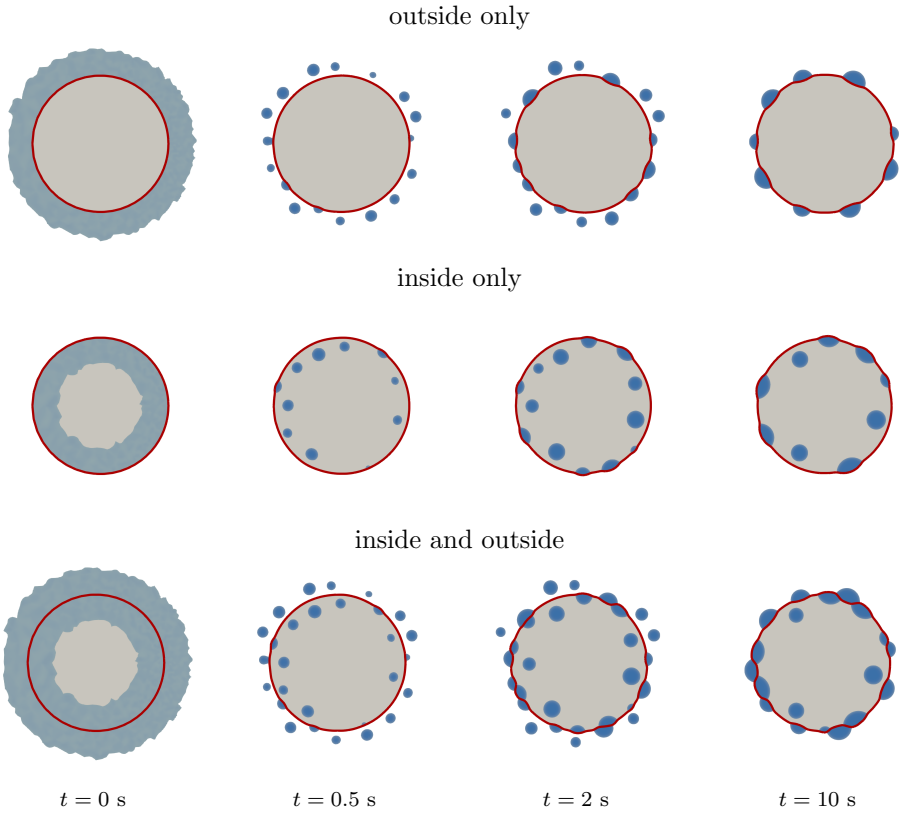

FIG. 4.6. *Droplet/ambient phase separation outside (top row), inside (middle row), and on both sides (bottom row) of a spherical membrane with contact angle* $\theta = 90°$. *In the light blue region at the initial state* $t = 0$ *s, the phase-field value is prescribed as random number* $\in [0.2, 0.3]$ *in each grid point. For the other time points, the droplets* ($\phi \geq 0.5$) *are illustrated in blue, the membrane in red, and the ambient fluids in white (outside) and gray (inside). After phase separation, coarsening sets in, such that small droplets vanish (Ostwald ripening) and larger droplets grow. All droplets interact with the membrane and with each other. Parameters:* $\sigma_f = 15\,\mu N/m$, $\sigma_0 = 30\,\mu N/m$, $\sigma_1 = 30\,\mu N/m$, $K_B = 8 \cdot 10^{-20}\,Nm$, $K_A = 5 \cdot 10^{-5}\ N/m$, $\varepsilon = 0.025\,\mu m$, *and* $P = 0\,m^2 s/kg$. *Initial membrane radius is* $2.5\,\mu m$. *Random initial values for* ϕ *are set in a ring with internal radius* $1.5\mu m$ *and/or external radius* $3.5\,\mu m$.

the membrane, the opposite behavior is observed. Droplets within and outside the membrane exhibit a tendency to attract each other, forming zigzag patterns along the membrane. In this case, the membrane slaloms between the droplets on either side, keeping droplets distant, thereby preventing further coarsening (Figures 4.7, 4.8, bottom row).

Phenomenologically, these results fit well to the experimental observations shown in [37] and supplementary movies S3 and S7. However, more detailed studies are necessary to understand the rich phenomenology and dynamics.

5. Conclusion and outlook. In this work we presented a first numerical method to simulate the continuum dynamics of droplets interacting with deformable membranes via wetting. We derived a thermodynamically consistent model which couples bulk hydrodynamics with capillary forces as well as bending, tension, and stretching of a thin membrane. The model combines the advantages of the phase-field method

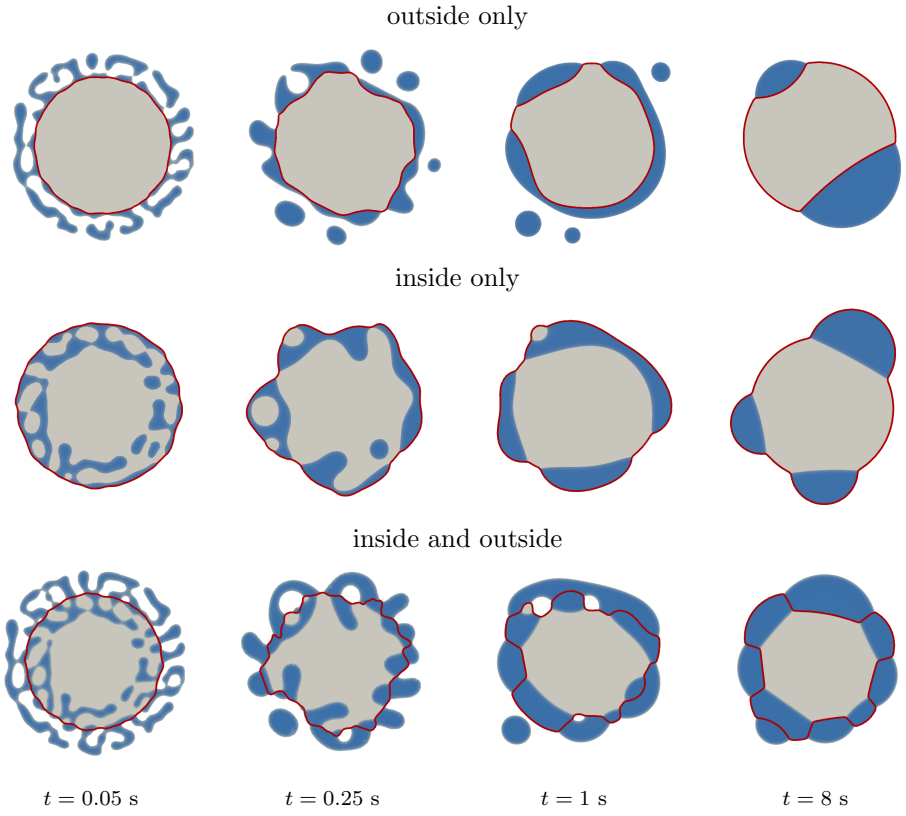

FIG. 4.7. *Droplet/ambient phase separation outside (top row), inside (middle row), and on both sides (bottom row) of a spherical membrane with contact angle* $\theta = 60°$. *The initial phase-field value is chosen to be a random number* $\in [0.2, 0.8]$ *on a ring around the membrane. The droplets* ($\phi \geq 0.5$) *are illustrated in blue, the membrane in red, and the ambient fluids in white (outside) and gray (inside). Parameters:* $\sigma_f = 30\,\mu N/m$, $\sigma_0 = 15\,\mu N/m$, $\sigma_1 = 30\,\mu N/m$, $K_B = 8 \cdot 10^{-20}\,Nm$, $K_A = 5 \cdot 10^{-5}\ N/m$, $\varepsilon = 0.025\,\mu m$, *and* $P = 0\,m^2 s/kg$. *Initial membrane radius is* $2.5\,\mu m$. *Random values for the phase field are set in a ring with internal radius* $1.5\mu m$ *and/or external radius* $3.5\,\mu m$.

for simulation of multiphase flow with those of the arbitrary Lagrangian-Eulerian (ALE) method for an explicit description of the elastic surface. Diffusivity of the liquid-liquid interface stabilizes the motion of the three-phase contact line, prevents contact line singularity and locking, and enables simulation of topological changes, such as droplet coalescence and break-up. On the other hand, the fitted finite element approach used to represent the membrane exactly resolves the discontinuities of pressure, viscosity, and liquid concentration across the membrane. Paired with adaptive mesh refinement, the method can accurately resolve the high curvature at the apparent membrane cusp observed at the three-phase contact line. In addition to grid movement by the ALE method, we introduced a remeshing algorithm which enables us to track large deformations of membranes up to a topological change.

We validated the method by comparing simulations for single droplets to the theoretical results of shape equations. Very good agreement was found, even for the high membrane curvature at the three-phase contact point. In a series of numerical tests, we illustrated the capabilities of the proposed method in 2D and 3D axisymmetric scenarios. We provided a first simulation of the dynamics of mutual droplet/membrane

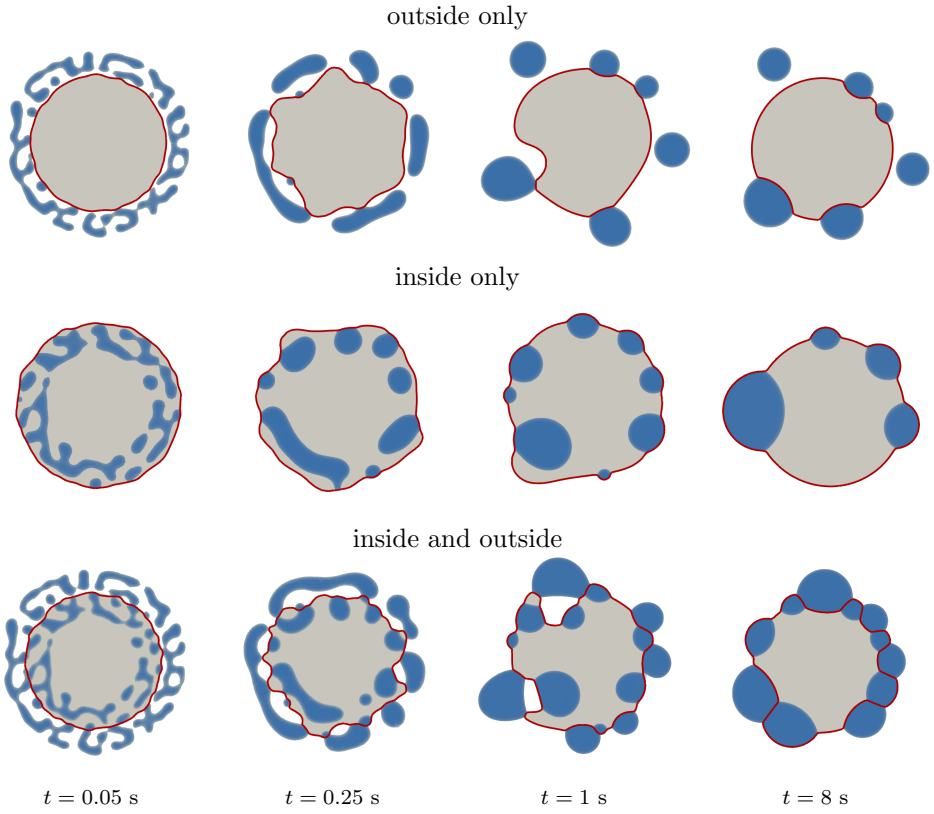

FIG. 4.8. *Droplet/ambient phase separation outside (top row), inside (middle row), and on both sides (bottom row) of a spherical membrane with contact angle* $\theta = 120°$. *The initial phase-field value is chosen to be a random number* $\in [0.2, 0.8]$ *on a ring around the membrane. The droplets* ($\phi \geq 0.5$) *are illustrated in blue, the membrane in red, and the ambient fluids in white (outside) and gray (inside). Parameters:* $\sigma_f = 30\,\mu N/m$, $\sigma_0 = 30\,\mu N/m$, $\sigma_1 = 15\,\mu N/m$, $K_B = 8 \cdot 10^{-20}$ *Nm,* $K_A = 5 \cdot 10^{-5}$ *N/m,* $\varepsilon = 0.025\,\mu m$, *and* $P = 0\,m^2 s/kg$. *Initial membrane radius is* $2.5\,\mu m$. *Random values for the phase field are set in a ring with internal radius* $1.5\mu m$ *and/or external radius* $3.5\,\mu m$.

remodeling. Moreover, an inverted endocytosis was simulated, where a smaller vesicle is absorbed into a larger drop by capillary forces. Additionally, we found an inverted Cheerios effect, evidenced by membrane-mediated repulsion of two droplets. Finally, we provided simulations of liquid-liquid phase separation around a vesicle membrane. The rich dynamics of which illustrate that numerical simulations are indispensable to systematically study these highly nonlinear phenomena.

Despite its potential for such toy problems, the presented method represents only a first step toward biologically relevant simulations of wetted membranes. The biological system comprises a variety of complex features which are not yet accounted for, including spontaneous curvature, line tension, and membrane binding [79]. Recognizing that bending stiffness generally depends on droplet contact [47] underlines the need for wetting-dependent bending stiffness. In this case also the Gaussian bending stiffness which is linked to K_B [30] is no longer negligible and poses conceptual challenges as additional coupling terms will arise in the phase-field evolution. Moreover, to address complex nonaxisymmetric geometries will require full 3D simulations, the computational effort of which demands parallelization, new remeshing strategies, and highly stable time stepping.

A clear limitation of the present method is given by the grid-based approach which excludes topological changes of the membrane. To handle membrane fusion and fission will require fundamentally different membrane representation and different numerical techniques.

Acknowledgments. The authors gratefully acknowledge computing time on the high-performance computer at the NHR Center at TU Dresden. This center is jointly supported by the Federal Ministry of Education and Research and the state governments participating in the NHR (www.nhr-verein.de/unsere-partner).

REFERENCES

[1] H. Abels, H. Garcke, and G. Grün, *Thermodynamically consistent, frame indifferent diffuse interface models for incompressible two-phase flows with different densities*, Math. Models Methods Appl. Sci., 22 (2011), 1150013.

[2] S. Aland, *Modelling of Two-Phase Flow with Surface Active Particles*, dissertation, Technische Universität Dresden, 2012, https://core.ac.uk/download/pdf/236367469.pdf.

[3] S. Aland, *Time integration for diffuse interface models for two-phase flow*, J. Comput. Phys., 262 (2014), pp. 58–71.

[4] S. Aland, S. Boden, A. Hahn, F. Klingbeil, M. Weismann, and S. Weller, *Quantitative comparison of Taylor flow simulations based on sharp-interface and diffuse-interface models*, Internat. J. Numer. Methods Fluids, 73 (2013), pp. 344–361.

[5] S. Aland and F. Chen, *An efficient and energy stable scheme for a phase-field model for the moving contact line problem*, Internat. J. Numer. Methods Fluids, 81 (2016), pp. 657–671.

[6] S. Aland, S. Egerer, J. Lowengrub, and A. Voigt, *Diffuse interface models of locally inextensible vesicles in a viscous fluid*, J. Comput. Phys., 277 (2014), pp. 32–47.

[7] S. Aland and D. Mokbel, *A unified numerical model for wetting of soft substrates*, Internat. J. Numer. Methods Engrg., 122 (2021), pp. 903–918.

[8] S. Aland and A. Voigt, *Benchmark computations of diffuse interface models for two-dimensional bubble dynamics*, Internat. J. Numer. Methods Engrg., 69 (2012), pp. 747–761.

[9] S. Alberti and A. A. Hyman, *Biomolecular condensates at the nexus of cellular stress, protein aggregation disease and ageing*, Nat. Rev. Mol. Cell Biol., 22 (2021), pp. 196–213.

[10] E. E. Ambroggio, G. S. C. Navarro, L. B. P. Socas, L. A. Bagatolli, and A. V. Gamarnik, *Dengue and zika virus capsid proteins bind to membranes and self-assemble into liquid droplets with nucleic acids*, J. Biol. Chem., 297 (2021), 101059.

[11] S. F. Banani, H. O. Lee, A. A. Hyman, and M. K. Rosen, *Biomolecular condensates: Organizers of cellular biochemistry*, Nat. Rev. Mol. Cell Biol., 18 (2017), pp. 285–298.

[12] J. Barrett, H. Garcke, and R. Nürnberg, *Parametric finite element approximations of curvature-driven interface evolutions*, Handb. Numer. Anal., 21 (2020), pp. 275–423.

[13] J. W. Barrett, H. Garcke, and R. Nürnberg, *A stable numerical method for the dynamics of fluidic membranes*, Numer. Math., 134 (2016), pp. 783–822.

[14] P. Bastian, G. Buse, and O. Sander, *Infrastructure for the coupling of dune grids*, in Numerical Mathematics and Advanced Applications 2009, G. Kreiss, P. Lötstedt, A. Målqvist, and M. Neytcheva, eds., Springer, Berlin, 2010, pp. 107–114.

[15] O. Beutel, R. Maraspini, K. Pombo-Garcia, C. Martin-Lemaitre, and A. Honigmann, *Phase separation of zonula occludens proteins drives formation of tight junctions*, Cell, 179 (2019), pp. 923–936.

[16] C. P. Brangwynne, C. R. Eckmann, D. S. Courson, A. Rybarska, C. Hoege, J. Gharakhani, F. Jülicher, and A. A. Hyman, *Germline p granules are liquid droplets that localize by controlled dissolution/condensation*, Science, 324 (2009), pp. 1729–1732.

[17] J. W. Cahn and J. E. Hilliard, *Free energy of a nonuniform system.* I. *Interfacial free energy*, J. Chem. Phys., 28 (2004), pp. 258–267.

[18] M. Cates, *Complex fluids: The physics of emulsions*, in Soft Interfaces: Lecture Notes of the Les Houches Summer School, Vol. 98, Oxford University Press, Oxford, UK, 2012, pp. 317–358.

[19] G. Chabouh, M. Mokbel, B. van Elburg, M. Versluis, T. Segers, S. Aland, C. Quilliet, and G. Coupier, *Coated microbubbles swim via shell buckling*, Commun. Eng., 2 (2023), pp. 2731–3395.

[20] K. J. Day, G. Kago, L. Wang, J. B. Richter, C. C. Hayden, E. M. Lafer, and J. C. Stachowiak, *Liquid-like protein interactions catalyse assembly of endocytic vesicles*, Nat. Cell Biol., 23 (2021), pp. 366–376.

[21] G. Dziuk, *Computational parametric Willmore flow*, Numer. Math., 111 (2008), 55.
[22] O. Et-Thakafy, N. Delorme, C. Gaillard, C. Mériadec, F. Artzner, C. Lopez, and F. Guyomarc'h, *Mechanical properties of membranes composed of gel-phase or fluid-phase phospholipids probed on liposomes by atomic force spectroscopy*, Langmuir, 33 (2017), pp. 5117–5126.
[23] E. Evans and W. Rawicz, *Entropy-driven tension and bending elasticity in condensed-fluid membranes*, Phys. Rev. Lett., 64 (1990), 2094–2097.
[24] R. Fettiplace and D. Haydon, *Water permeability of lipid membranes*, Physiol. Rev., 60 (1980), pp. 510–550.
[25] C. Geuzaine and J.-F. Remacle, *Gmsh: A 3-D finite element mesh generator with built-in pre- and post-processing facilities*, Internat. J. Numer. Methods Engrg., 79 (2009), pp. 1309–1331.
[26] R. Ghosh, V. Satarifard, and R. Lipowsky, *Different pathways for engulfment and endocytosis of liquid droplets by nanovesicles*, Nat. Commun., 14 (2023), 615.
[27] B. Gouveia, Y. Kim, J. W. Shaevitz, S. Petry, H. A. Stone, and C. P. Brangwynne, *Capillary forces generated by biomolecular condensates*, Nature, 609 (2022), pp. 255–264.
[28] S. Gross and A. Reusken, *An extended pressure finite element space for two-phase incompressible flows with surface tension*, J. Comput. Phys., 224 (2007), pp. 40–58.
[29] F. Guillén-González and G. Tierra, *Unconditionally energy stable numerical schemes for phase-field vesicle membrane model*, J. Comput. Phys., 354 (2018), pp. 67–85.
[30] M. Hu, J. J. Briguglio, and M. Deserno, *Determining the Gaussian curvature modulus of lipid membranes in simulations*, Biophys. J., 102 (2012), pp. 1403–1410.
[31] P. Iyer, G. Gompper, and D. A. Fedosov, *Dynamic shapes of floppy vesicles enclosing active Brownian particles with membrane adhesion*, Soft Matter, 19 (2023), pp. 3436–3449.
[32] D. Jacqmin, *Contact-line dynamics of a diffuse fluid interface*, J. Fluid Mech., 402 (2000), pp. 57–88.
[33] S. Karpitschka, A. Pandey, L. A. Lubbers, J. H. Weijs, L. Botto, S. Das, B. Andreotti, and J. H. Snoeijer, *Liquid drops attract or repel by the inverted cheerios effect*, Proc. Natl. Acad. Sci. USA, 113 (2016), pp. 7403–7407.
[34] J. Kim, *Phase-field models for multi-component fluid flows*, Commun. Comput. Phys., 12 (2015).
[35] T. Krüger, F. Varnik, and D. Raabe, *Efficient and accurate simulations of deformable particles immersed in a fluid using a combined immersed boundary lattice Boltzmann finite element method*, Comput. Math. Appl., 61 (2011), pp. 3485–3505.
[36] H. Kusumaatmaja and R. Lipowsky, *Droplet-induced budding transitions of membranes*, Soft Matter, 7 (2011), pp. 6914–6919.
[37] H. Kusumaatmaja, A. I. May, M. Feeney, J. F. McKenna, N. Mizushima, L. Frigerio, and R. L. Knorr, *Wetting of phase-separated droplets on plant vacuole membranes leads to a competition between tonoplast budding and nanotube formation*, Proc. Natl. Acad. Sci. USA, 118 (2021), e2024109118.
[38] H. Kusumaatmaja and J. Yeomans, *Modeling contact angle hysteresis on chemically patterned and superhydrophobic surfaces*, Langmuir, 23 (2007), pp. 6019–6032.
[39] A. Laadhari, P. Saramito, and C. Misbah, *Computing the dynamics of biomembranes by combining conservative level set and adaptive finite element methods*, J. Comput. Phys., 263 (2014), pp. 328–352.
[40] C.-H. Lee, W.-C. Lin, and J. Wang, *All-optical measurements of the bending rigidity of lipid-vesicle membranes across structural phase transitions*, Phys. Rev. E, 64 (2001), 020901.
[41] J. E. Lee, P. I. Cathey, H. Wu, R. Parker, and G. K. Voeltz, *Endoplasmic reticulum contact sites regulate the dynamics of membraneless organelles*, Science, 367 (2020), eaay7108.
[42] R. Lipowsky, *Understanding Giant Vesicles: A Theoretical Perspective*, CRC Press, Boca Raton, FL, 2019, pp. 73–168.
[43] R. Lipowsky, *Multispherical shapes of vesicles highlight the curvature elasticity of biomembranes*, Adv. Colloid Interface Sci., 301 (2022), 102613.
[44] R. Lipowsky, *Remodeling of biomembranes and vesicles by adhesion of condensate droplets*, Membranes, 13 (2023), 223.
[45] T. Lu, S. Liese, L. Schoenmakers, C. A. Weber, H. Suzuki, W. T. S. Huck, and E. Spruijt, *Endocytosis of coacervates into liposomes*, J. Amer. Chem. Soc., 144 (2022), pp. 13451–13455.
[46] A. Mangiarotti, N. Chen, Z. Zhao, R. Lipowsky, and R. Dimova, *Wetting and complex remodeling of membranes by biomolecular condensates*, Nat. Commun., 14 (2023), 2809.
[47] A. Mangiarotti, M. Siri, N. W. Tam, Z. Zhao, L. Malacrida, and R. Dimova, *Biomolecular condensates modulate membrane lipid packing and hydration*, Nat. Commun., 14 (2023), 6081.

[48] D. Mokbel, S. Aland, and S. Karpitschka, *Stick-slip contact line motion on Kelvin-Voigt model substrates*, Europhys. Lett., 139 (2022), 33002.
[49] M. Mokbel and S. Aland, *An ALE method for simulations of axisymmetric elastic surfaces in flow*, Internat. J. Numer. Methods Fluids, 92 (2020), pp. 1604–1625.
[50] M. Mokbel, K. Hosseini, S. Aland, and E. Fischer-Friedrich, *The Poisson ratio of the cellular actin cortex is frequency-dependent*, Biophys. J., 118 (2020), pp. 1968–1976.
[51] M. Mokbel, D. Mokbel, A. Mietke, N. Träber, S. Girardo, O. Otto, J. Guck, and S. Aland, *Numerical simulation of real-time deformability cytometry to extract cell mechanical properties*, ACS Biomater. Sci. Eng., 3 (2017), pp. 2962–2973.
[52] S. Mondal and T. Baumgart, *Membrane reshaping by protein condensates*, Biochimica et Biophysica Acta (BBA) Biomembranes, 1865 (2023), 184121.
[53] U. Moran, R. Phillips, and R. Milo, *Snapshot: Key numbers in biology*, Cell, 141 (2010), pp. 1262–1262.
[54] H. Noguchi and G. Gompper, *Fluid vesicles with viscous membranes in shear flow*, Phys. Rev. Lett., 93 (2004), 258102.
[55] K. Olbrich, W. Rawicz, D. Needham, and E. Evans, *Water permeability and mechanical strength of polyunsaturated lipid bilayers*, Biophys. J., 79 (2000), pp. 321–327.
[56] K. C. Ong and M.-C. Lai, *An immersed boundary projection method for simulating the inextensible vesicle dynamics*, J. Comput. Phys., 408 (2020), 109277.
[57] M. Pepona, A. Shek, C. Semprebon, T. Krüger, and H. Kusumaatmaja, *Modeling ternary fluids in contact with elastic membranes*, Phys. Rev. E, 103 (2021), 022112.
[58] L. Picas, F. Rico, and S. Scheuring, *Direct measurement of the mechanical properties of lipid phases in supported bilayers*, Biophys. J., 102 (2012), pp. L01–L03.
[59] T. Quail, S. Golfier, M. Elsner, K. Ishihara, V. Murugesan, R. Renger, F. Jülicher, and J. Brugués, *Force generation by protein–DNA co-condensation*, Nat. Phys., 17 (2021), pp. 1007–1012.
[60] L. E. Reichl, *A Modern Course in Statistical Physics*, John Wiley & Sons, New York, 2016.
[61] A. Rosolen, C. Peco, and M. Arroyo, *An adaptive meshfree method for phase-field models of biomembranes*, J. Comput. Phys., 249 (2013), pp. 303–336.
[62] T. Ruiz-Herrero, T. G. Fai, and L. Mahadevan, *Dynamics of growth and form in prebiotic vesicles*, Phys. Rev. Lett., 123 (2019), 038102.
[63] M. Sacerdote and J. Szostak, *Semipermeable lipid bilayers exhibit diastereoselectivity favoring ribose*, Proc. Natl. Acad. Sci. USA, 102 (2005), pp. 6004–6008.
[64] D. Salac and M. Miksis, *A level set projection model of lipid vesicles in general flows*, J. Comput. Phys., 230 (2011), pp. 8192–8215.
[65] V. Satarifard and R. Lipowsky, *Mutual remodeling of interacting nanodroplets and vesicles*, Commun. Phys., 6 (2023), 6.
[66] J. Shen, X. Yang, and H. Yu, *Efficient energy stable numerical schemes for a phase field moving contact line model*, J. Comput. Phys., 284 (2015), pp. 617–630.
[67] L. Shi, T.-W. Pan, and R. Glowinski, *Three-dimensional numerical simulation of red blood cell motion in poiseuille flows*, Internat. J. Numer. Methods Fluids, 76 (2014), pp. 397–415.
[68] Y. Shin and C. P. Brangwynne, *Liquid phase condensation in cell physiology and disease*, Science, 357 (2017), eaaf4382.
[69] W. T. Snead, A. P. Jalihal, T. M. Gerbich, I. Seim, Z. Hu, and A. S. Gladfelter, *Membrane surfaces regulate assembly of ribonucleoprotein condensates*, Nat. Cell Biol., 24 (2022), pp. 461–470.
[70] X. Su, J. A. Ditlev, E. Hui, W. Xing, S. Banjade, J. Okrut, D. S. King, J. Taunton, M. K. Rosen, and R. D. Vale, *Phase separation of signaling molecules promotes t cell receptor signal transduction*, Science, 352 (2016), pp. 595–599.
[71] M. Tsanai, P. J. M. Frederix, C. F. E. Schroer, P. C. T. Souza, and S. J. Marrink, *Coacervate formation studied by explicit solvent coarse-grain molecular dynamics with the Martini model*, Chem. Sci., 12 (2021), pp. 8521–8530.
[72] E. H. van Brummelen, M. S. Roudbari, G. Şimşek, and K. G. van der Zee, *Binary-fluid–solid interaction based on the Navier–Stokes–Cahn–Hilliard equations*, in Fluid-Structure Interaction, De Gruyter, Berlin, 2017, pp. 283–328.
[73] J. van der Waals, *The thermodynamic theory of capillarity flow under the hypothesis of continuous variation in density*, J. Stat. Phys., 20 (1893), pp. 200–244.
[74] H. Wang, F. M. Kelley, D. Milovanovic, B. S. Schuster, and Z. Shi, *Surface tension and viscosity of protein condensates quantified by micropipette aspiration*, Biophys. Rep., 1 (2021), 100011.
[75] D. Wirtz, *Particle-tracking microrheology of living cells: Principles and applications*, Ann. Rev. Biophys., 38 (2009), pp. 301–326.

[76] J. Yang, Y. Li, and J. Kim, *Totally decoupled implicit–explicit linear scheme with corrected energy dissipation law for the phase-field fluid vesicle model*, Comput. Methods Appl. Mech. Engrg., 399 (2022), 115330.
[77] X. Yang and L. Ju, *Efficient linear schemes with unconditional energy stability for the phase field elastic bending energy model*, Comput. Methods Appl. Mech. Engrg., 315 (2017), pp. 691–712.
[78] X. Yang and H. Yu, *Efficient second order unconditionally stable schemes for a phase field moving contact line model using an invariant energy quadratization approach*, SIAM J. Sci. Comput., 40 (2018), pp. B889–B914.
[79] X. Zhao, G. Bartolucci, A. Honigmann, F. Jülicher, and C. A. Weber, *Thermodynamics of wetting, prewetting and surface phase transitions with surface binding*, New J. Phys., 23 (2021), 123003.
[80] Y. G. Zhao and H. Zhang, *Phase separation in membrane biology: The interplay between membrane-bound organelles and membraneless condensates*, Dev. Cell, 55 (2020), pp. 30–44.
[81] G. Zhu, J. Kou, J. Yao, A. Li, and S. Sun, *A phase-field moving contact line model with soluble surfactants*, J. Comput. Phys., 405 (2020), 109170.